

# Generating stable solitary waves with a piston-type wavemaker

Vivek Francis<sup>a,b,\*</sup>, Balaji Ramakrishnan<sup>a</sup>, Murray Rudman<sup>b</sup>, Alireza Valizadeh<sup>b,c</sup>

<sup>a</sup> Department of Civil Engineering, Indian Institute of Technology Bombay, Mumbai, 400076, India

<sup>b</sup> Department of Mechanical & Aerospace Engineering, Monash University, Melbourne, VIC, 3800, Australia

<sup>c</sup> DHI Water and Environment Pty Ltd., Gold Coast, QLD, 4217, Australia

## ARTICLE INFO

### Keywords:

Solitary wave  
Physical modeling  
Wave generation  
Piston-type wavemaker  
Numerical modeling  
SPH

## ABSTRACT

The generation of stable and pure solitary waves in large-scale experimental flumes and numerical models is the focus of this study. Such waves give a better description of the target wave amplitude, has minimal amplitude dissipation during propagation and has negligible trailing waves. In the present study, the two solitary wave generation methodologies, namely, Goring's Method (GM) and the Malek-Mohammadi and Testik Method (MMTM), described in Goring (1979) and Malek-Mohammadi and Testik (2010) respectively, have been used to examine the solitary wave solutions of Boussinesq, Rayleigh, Grimshaw and Fenton, both experimentally and numerically for three different relative wave height ( $\epsilon$ ), ratios of 0.1, 0.3 and 0.6. Numerical modeling is done within a Smoothed Particle Hydrodynamics (SPH) framework developed in Valizadeh and Rudman (2017). For each  $\epsilon$  value, we have compared the experimental and numerical results in terms of the free surface profiles and the phase speeds to give recommendations for the solitary wave solution and the generation methodology that demonstrates the best performance. Our results indicate that the Rayleigh solitary wave solution gives more accurate profiles in both experiments and numerical simulations. With respect to wave generation methodology, the MMTM gives the best results in the experiments, whereas, the GM describes the target waves better in our numerical SPH simulations.

## 1. Introduction

Tsunami waves pose a threat to the coastal zone and numerous studies have been carried out in the past to understand them. To model a tsunami wave, solitary waves have often been used (Synolakis, 1987; Hsiao and Lin, 2010; Liang et al., 2013; Gedik et al., 2005; Goseberg et al., 2013) as an approximation that contains some of its important features, especially their stable form and the fact that a leading tsunami wave after having traveled long distances emerges as a solitary wave (Yeh et al., 1994).

The propagation of surface water waves are governed by the Euler equations, but, owing to their complexity, simpler approximate equations have been derived from them. The Boussinesq equations are a set of first-order equations derived from the full Euler equations and have a particular solitary wave solution which is similar in form to the approximate solutions developed by Boussinesq in (Boussinesq, 1871) and Lord Rayleigh in (Rayleigh, 1876). In order to obtain solitary wave solutions directly from the Euler equations, several approximate higher-order theories have also been developed over the years (Teng,

1997). These include formulations by approximations to shallow water theories (see (Clamond and Germain, 1999), (Temperville, 1985)), Grimshaw's third-order solution (Grimshaw, 1971) and Fenton's ninth-order solution (Fenton, 1972).

Solitary waves are normally generated, both experimentally and numerically, by employing a piston-type wavemaker and based on the theory developed by Goring in (Goring, 1979). The basis of solitary wave generation using Goring's method (GM) is to match the depth-averaged horizontal water particle velocity near to the wavemaker,  $\bar{u}(X, t)$ , with the velocity of the wavemaker,  $dX/dt$ . This formula, used by Goring in (Goring, 1979), is expressed as:

$$dX / dt = \bar{u}(X, t) \quad (1)$$

where  $X$  is the position of the wavemaker at time  $t$ . The depth-averaged horizontal water particle velocity under a solitary wave is assumed to be constant throughout the depth and is estimated (Svendsen, 1974) from the following equation:

\* Corresponding author. Department of Civil Engineering, Indian Institute of Technology Bombay, Mumbai, 400076, India.

E-mail addresses: [vivek.francis@monash.edu](mailto:vivek.francis@monash.edu) (V. Francis), [rbalaji@civil.iitb.ac.in](mailto:rbalaji@civil.iitb.ac.in) (B. Ramakrishnan), [murray.rudman@monash.edu](mailto:murray.rudman@monash.edu) (M. Rudman), [alireza.valizadeh@monash.edu](mailto:alireza.valizadeh@monash.edu) (A. Valizadeh).

<https://doi.org/10.1016/j.coastaleng.2020.103633>

Received 26 July 2019; Received in revised form 20 December 2019; Accepted 2 January 2020

Available online 9 January 2020

0378-3839/© 2020 Elsevier B.V. All rights reserved.

$$\bar{u}(X, t) = \frac{c\eta(X, t)}{d + \eta(X, t)} \quad (2)$$

where  $c$  is the theoretical celerity of the wave,  $d$  is still water depth, and  $\eta$  is the water surface elevation. Upon integrating Eq. (1) in time, the wavemaker trajectory can be obtained. From theory, it is expected that the generated solitary wave has the following form:

$$\eta(x, t) = A f(\beta\theta) \quad (3)$$

where  $A$  is the amplitude of the solitary wave,  $\beta$  is the outskirts decay coefficient and  $\theta$  is the phase angle. Our objective in this study is to generate stable and pure solitary waves. A stable and pure solitary wave retains its shape with a steady amplitude during propagation with negligible trailing waves after having traveled long distances.

Using GM, Katell and Eric (2002) experimentally generated Boussinesq and Rayleigh-type solitary waves along with solutions derived by linearizing the Lagrangian formulation in the first-order and second-order shallow water theories, for a range of relative wave height ( $\epsilon$ ), between 0.1 and 0.6. They reported that, on comparing water surface elevations, the Rayleigh-type solitary waves are more stable and have amplitude characteristics which are closer in agreement to the target solitary wave. They also reported that Boussinesq-type solitary waves generated by GM were found to be steady only after having traveled a distance of around eighty times the water depth from the wavemaker, while the Rayleigh-type solitary waves become stable at a distance of around twenty times the water depth. Both Goring (1979) and Katell and Eric (2002) have recorded that all solitary waves generated using GM are always followed by an oscillatory tail. For a Boussinesq-type solitary wave, the amplitude of the trailing waves are reported to be 6–12% of the main pulse (see (Goring, 1979)), while for a Rayleigh-type solitary wave it was 3–8% of the generated wave (see (Katell and Eric, 2002)). The experimental findings in (Katell and Eric, 2002) have been numerically confirmed using a weakly compressible ‘DualSPHysics’ SPH model in (Altomare et al., 2017). Wu et al., in (Wu et al., 2014), have studied numerically the generation and propagation of Boussinesq, Rayleigh, Grimshaw and Fenton-type solitary waves, by using GM in a meshfree potential flow model. They concluded from their study that Fenton-type solitary wave gives the best performance for  $\epsilon$  values up to 0.4. Recently, Wu et al. (2016), have validated the numerical study in (Wu et al., 2014) by physical experiments, and they have confirmed that Fenton-type solitary wave gives the most stable solitary waves. The solitary wave solutions discussed in (Katell and Eric, 2002) and (Wu et al., 2014) have also been tested numerically in an Incompressible Smoothed Particle Hydrodynamics (ISPH) model by using GM (Farhadi et al., 2016). The ISPH model results corroborate those presented in (Wu et al., 2014).

While GM for generating a solitary wave is the most often used (Valizadeh and Rudman, 2017; Synolakis, 1987; Hsiao and Lin, 2010; Katell and Eric, 2002; Farhadi et al., 2016), an alternate methodology for generating a solitary wave based on the horizontal movement of a piston-type wavemaker has been developed by Malek-Mohammadi and Testik in (Malek-Mohammadi and Testik, 2010). In this method, henceforth referred to as ‘MMTM’, the evolving nature of the wave during the wave generation process has been accounted for. The GM, on the other hand, assumes a solitary wave of constant celerity and permanent form during the wave generation stage. According to the MMTM, the authors have assumed that as the wavemaker piston moves, pushing the water column in front, it produces small surges at each instant, all of which adds up to eventually form the desired wave. Therefore, during its generation, the solitary wave propagates with a celerity parameter that changes with time,  $c_u(t)$ . The creation of surges during the wave generation process was considered only during the formation of the leading half of the solitary wave and the trailing half of the wave profile is generated with the constant celerity of the last surge that forms the peak of the solitary wave crest. Based on these

considerations, for generating the leading half of the solitary wave, the unsteady celerity is determined from the following formulation:

$$c_u(t) = \sqrt{g \left( d + \frac{\eta_s}{2} \right) \left( 1 + \frac{\eta_s}{d} \right)} \quad (4)$$

where  $\eta_s$  is the instantaneous surge height at the location of the moving wavemaker and  $g$  is the gravitational acceleration. The trailing half of the wave profile is generated with a constant celerity by substituting  $\eta_s = A$  in Eq. (4). The wavemaker velocity is then calculated at each instant by substituting Eq. (4) in Eq. (2), and the wavemaker trajectory is determined by integrating the resulting expression in time. On the basis of their experimental study involving Boussinesq and Rayleigh-type solitary waves in a range of  $\epsilon$  between 0.3 and 0.6 (see (Malek-Mohammadi and Testik, 2010)), Malek-Mohammadi and Testik concluded that the waves generated using the MMTM are superior to the waves generated using GM in terms of wave height, wave celerity and wave profile shape. Significantly, they reported that the solitary waves were established at much shorter distances—even at a distance of ten times the water depth from the wavemaker—and were less dispersive. The authors in (Malek-Mohammadi and Testik, 2010) have recorded the Rayleigh-type waves to represent the target solitary waves better than the Boussinesq-type, similar to the observations made by Katell and Eric (2002). Results in (Malek-Mohammadi and Testik, 2010) showed that solitary waves generated using the MMTM are also followed by an oscillatory tail. But, the amplitudes of these are smaller than those generated by GM, with the Rayleigh-type waves resulting in the smallest depressions of all.

Goring’s method makes use of the wavemaker velocity formula as expressed in Eq. (1). By evaluating the trajectory equations at time  $t = \pm\infty$ , the stroke ( $S$ ), of the wavemaker can be found:

$$X(\pm\infty) = \pm S/2 \quad (5)$$

Therefore, the wavemaker moves from  $-S/2$  at time  $t = -\infty$  to  $+S/2$  at time  $t = +\infty$ . Theoretically, the duration of the wavemaker motion ( $\tau$ ), is therefore infinite. However, for practical purposes, it is assumed that when the wavemaker reaches 0.9999 times its total stroke length, the solitary wave is completely generated, thereby yielding:

$$\tau = \frac{4}{\beta c} [\tanh^{-1}(0.9999) + \epsilon] \quad (6)$$

In the MMTM, the wavemaker velocity is determined by substituting Eq. (4) in Eq. (2), and from which the wavemaker trajectory equations are calculated. Since the outskirts decay coefficient of the solitary wave remains unchanged in the MMTM, the total stroke of the wavemaker is equal to the one used in Goring’s method. In order to make direct comparisons between methods, Malek-Mohammadi and Testik calculated the duration of wavemaker motion based on Eq. (6). Fig. 1 compares the wavemaker trajectory and velocity using the two methods for generating a Rayleigh-type solitary wave. In this case, it can be seen that in both methods the wavemaker trajectory and velocities are similar, with the peak wavemaker velocity in the MMTM 7.22% higher than GM.

For both methods, the intercepts of the characteristics associated with the leading and trailing edges of the solitary wave with the time axis,  $\pm\tau/2$ , occur at  $\pm\infty$ . Therefore, in order to have a wavemaker trajectory that moves from rest in a forward direction, the origin of the wavemaker trajectory,  $X(0)$ , is shifted to the point  $(-S/2, -\tau/2)$  in the  $x$ - $t$  plane.

A practical concern which arises during the experimental generation of solitary waves is that, usually for larger water depths, when the dimensionless amplitude of a solitary wave ( $\epsilon$ ), goes beyond 0.4, the finite stroke of the wavemaker piston will prevent the generation of steeper solitary waves in most wave generation systems ((Katell and Eric, 2002)). This limitation has a practical significance because the range over which solitary wave experiments are normally carried out is often under weak to moderate nonlinearity ( $\epsilon \leq 0.4$ ) only. To address

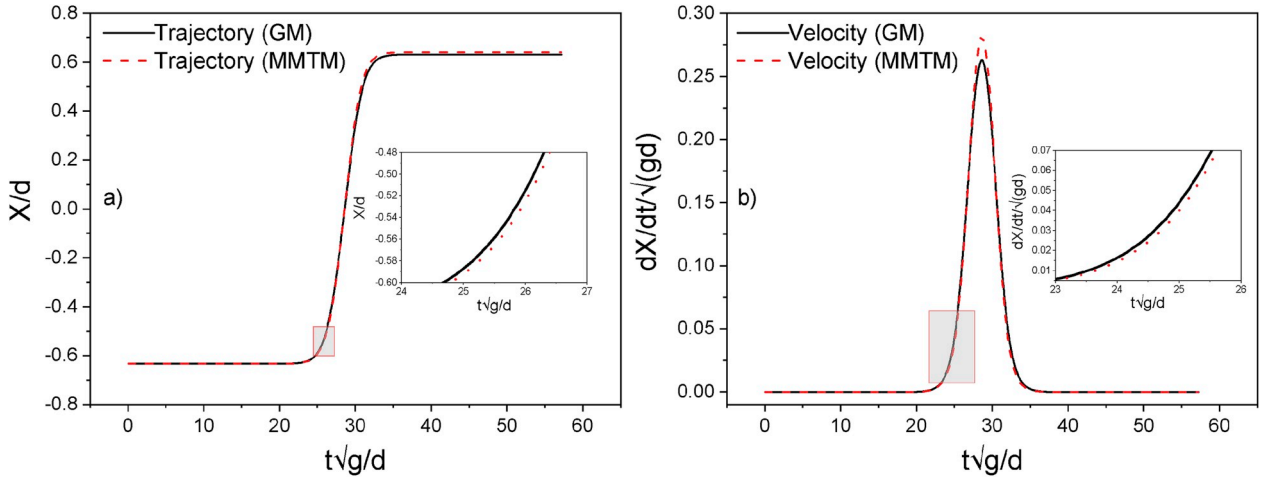


Fig. 1. Wavemaker piston (a) trajectory and (b) velocity for generating a typical Rayleigh solitary wave ( $\epsilon = 0.3$ ) using the GM and MMTM methods.

this limitation, in our study, we have used a SPH-based Weakly Compressible Smoothed Particle Hydrodynamics (WCSPH) model described in (Valizadeh and Rudman, 2017) for the generation of various solitary wave solutions using GM and MMTM.

The aim of this study is to generate the most stable and pure solitary waves using a piston-type wavemaker in both experiments and numerical simulations. Inspired by the experimental investigation conducted in (Katell and Eric, 2002), (Malek-Mohammadi and Testik, 2010), and (Wu et al., 2016), four solitary wave solutions, namely, Boussinesq's first order solitary wave solution (see (Boussinesq, 1871)), Rayleigh's first order solitary wave solution (refer (Rayleigh, 1876)), Grimshaw's third order solitary wave solution (given in (Grimshaw, 1971)) and Fenton's ninth order solitary wave solution (from (Fenton, 1972)), are tested in this study using the two wave generation methodologies. The two methodologies for generating solitary waves are based on fundamentally different assumptions and their application to the four different solitary wave solutions are discussed in this study. Solitary waves based on the Korteweg-de Vries equation (KdV) rely on both long waves and small amplitude assumptions and since these solitary waves have been established to be of lower quality than the Rayleigh and Boussinesq-type solutions in (Katell and Eric, 2002), (Altomare et al., 2017) and (Farhadi et al., 2016), they have not been considered here.

The captured waveform, from both experiments and numerical simulations, have been analyzed in terms of the following parameters: amplitude, phase speed, stability and profile shape of the main pulse and the amplitude of the trailing waves. Similar to the study conducted in (Katell and Eric, 2002), the Byatt-Smith numerical solution given in (Byatt-Smith, 1970) has been used as a benchmark against which the performance of all solitary wave solutions was evaluated. The numerical solution for the solitary wave derived by Byatt-Smith in (Byatt-Smith, 1970) comes from an exact integro-differential equation for steady surface waves within potential flow theory, and is considered to be the most accurate in terms of the profiles and properties of solitary waves. We would like to highlight that no experiments or simulations were performed using the Byatt-Smith solution as it has been reported to be not very practical (Katell and Eric, 2002).

The novelty of this study lies in its evaluation through both experiments and numerical WCSPH simulations of the stability and purity of different solitary wave solutions generated using two different methods, i.e. the GM and the MMTM, at large distances from the wave generation zone. Therefore, the main objective of this paper is to determine the wave generation mechanism and the theoretical solitary wave solution that results in a solitary wave with the most fidelity.

## 2. The four solitary wave solutions

All four solitary wave solutions have the form given in Eq. (3). However, they differ on how the free surface displacement ( $\eta$ ), the wave celerity ( $c$ ), and the outskirts decay coefficient ( $\beta$ ), are defined. In this study,  $\eta$ ,  $c$  and  $\beta$  will be labeled with the following subscripts:  $B$  for Boussinesq-type waves,  $R$  for Rayleigh-type waves,  $G$  for Grimshaw-type waves and  $F$  for Fenton-type waves.

### 2.1. Boussinesq: first order

The first-order Boussinesq solitary wave solution has the following functional form:

$$\eta_B = A \operatorname{sech}^2 \left( \frac{\beta_B (c_B t - X)}{2} \right) \quad (7)$$

Based on the results presented in (Daily and Stephan, 1952), Goring in (Goring, 1979) used the following values for  $\beta_B$  and  $c_B$  in Eq. (7):

$$\beta_B = \sqrt{\frac{3A}{d^3}} \quad (8)$$

$$c_B = \sqrt{g(A + d)} \quad (9)$$

Boussinesq-type solitary waves generated using these values are reported to be severely damped in (Goring, 1979) with less agreement between the generated and theoretical wave amplitudes at increasing values of  $\epsilon$ . Goring, in (Goring, 1979), has also commented on the presence of dispersive oscillatory trailing waves that follow the main peak of the solitary wave when generated by piston-type wavemakers.

### 2.2. Rayleigh: first order

The first-order Rayleigh solitary wave solution has the following form:

$$\eta_R = A \operatorname{sech}^2 \left( \frac{\beta_R (c_R t - X)}{2} \right) \quad (10)$$

where,

$$\beta_R = \frac{1}{d} \sqrt{\frac{3A}{A + d}} \quad (11)$$

$$c_R = \sqrt{g(A + d)} \quad (12)$$

By examining Eq. (11) it can be seen that the outskirts decay coefficient is different from that used for generating a Boussinesq-type

solitary wave, given by Eq. (8). But the free surface profile description and the celerity are the same as the Boussinesq solution.

### 2.3. Grimshaw: third order

The third-order Grimshaw solitary wave has the following form:

$$\eta_G = d \left[ \epsilon S^2 - \frac{3}{4} \epsilon^2 S^2 T^2 + \epsilon^3 \left( \frac{5}{8} S^2 T^2 - \frac{101}{80} S^4 T^2 \right) \right] \quad (13)$$

where,

$$S = \text{sech} \left( \frac{\beta_G (X - ct)}{d} \right) \quad (14)$$

$$T = \tanh \left( \frac{\beta_G (X - ct)}{d} \right) \quad (15)$$

and

$$\beta_G = \sqrt{\frac{3\epsilon}{4}} \left( 1 - \frac{5}{8} \epsilon + \frac{71}{128} \epsilon^2 \right) \quad (16)$$

$$c_G = \sqrt{gd} \left( 1 + \epsilon - \frac{1}{20} \epsilon^2 - \frac{3}{70} \epsilon^3 \right)^{0.5} \quad (17)$$

### 2.4. Fenton: ninth order

Fenton in (Fenton, 1972) has described a ninth-order solution of the solitary wave, with the coefficients determined numerically, the free surface elevation of which is defined in the following way:

$$\eta_F = d(\eta_1 S^2 + \eta_2 S^4 + \eta_3 S^6 + \eta_4 S^8 + \eta_5 S^{10} + \eta_6 S^{12} + \eta_7 S^{14} + \eta_8 S^{16} + \eta_9 S^{18}) \quad (18)$$

where,

$$S = \text{sech} \left( \frac{\beta_F (c_F t - X)}{2} \right) \quad (19)$$

and

$$\beta_F = \frac{3\epsilon}{d} (1 + \beta_1 \epsilon + \beta_2 \epsilon^2 + \beta_3 \epsilon^3 + \beta_4 \epsilon^4 + \beta_5 \epsilon^5 + \beta_6 \epsilon^6 + \beta_7 \epsilon^7 + \beta_8 \epsilon^8 + \beta_9 \epsilon^9) \quad (20)$$

$$c_F = \sqrt{gd} (1 + c_1 \epsilon + c_2 \epsilon^2 + c_3 \epsilon^3 + c_4 \epsilon^4 + c_5 \epsilon^5 + c_6 \epsilon^6 + c_7 \epsilon^7 + c_8 \epsilon^8 + c_9 \epsilon^9) \quad (21)$$

The formulae to determine the coefficient values  $\eta_1$  to  $\eta_9$ ,  $\beta_1$  to  $\beta_9$  and  $c_1$  to  $c_9$  in Eqs. (18), (20) and (21) can be found in Table 1 of (Fenton, 1972).

## 3. Properties of the four solutions

In this section, we present and compare the properties of the different solitary wave solutions. We have used the GM generation method to highlight the relevant theoretical properties associated with the four solutions.

The theoretical stroke of the wavemaker ( $S$ ) for the different solitary wave solutions is compared in Fig. 2. As expected, solitary waves of higher amplitudes require a greater volume of water to be pushed. It can also be seen from the figure that the stroke of the wavemaker for Grimshaw's solution and Fenton's solution are similar for low values of  $\epsilon$ , and, as the nonlinearity of the wave increases ( $\epsilon > 0.3$ ), a higher volume of water needs to be pushed by the latter. It is also clear that the Rayleigh solution has a larger total stroke for all  $\epsilon$ , when compared to the other three solutions. The non-dimensional wavemaker velocities

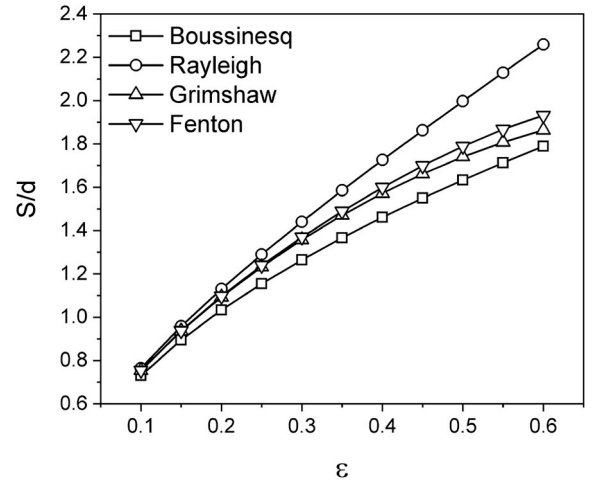


Fig. 2. Theoretical non-dimensionalized maximum paddle displacement for the different solitary wave solutions.

corresponding to the four solutions for generating a solitary wave of  $\epsilon = 0.3$  is shown and compared in Fig. 3. As can be seen, the wavemaker velocity has a wider bell-shape when the Rayleigh solution is applied. Thus it can be inferred that the Rayleigh solution pushes a larger volume of water than the others. A solitary wave solution that causes larger water volume to be pushed by the wavemaker may result in profiles which undergo less damping than those resulting from low water volume.

Since the theoretical wave celerity is used to determine the velocity of the wavemaker, the properties of the generated wave can be expected to be dependent on the chosen celerity value. Based on Eqs. ((9), (12), (17) and (21)), each solitary wave solution results in wave celerity values specific to the theory used. Since Eqs. (9) and (12) are identical, the Boussinesq and Rayleigh phase speeds determined by them are the same. Here, in Fig. 4, we have used the numerical estimation of the dimensionless phase speed by Byatt-Smith given in (Byatt-Smith and Longuet-Higgins, 1976) as a reference for comparing the different celerities. It can be seen that when  $\epsilon$  is less than 0.3, all four solutions yield phase speeds that match well with the Byatt-Smith estimates. For higher amplitude solitary waves, the Fenton solution and the Grimshaw solution gives phase speeds that are closer to the Byatt-Smith estimates, followed by the first order solutions of Boussinesq and Rayleigh.

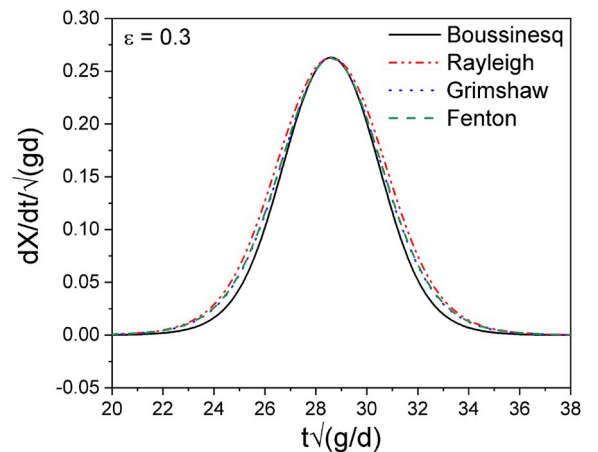


Fig. 3. Theoretical non-dimensionalized wavemaker velocities for the different solitary wave solutions.



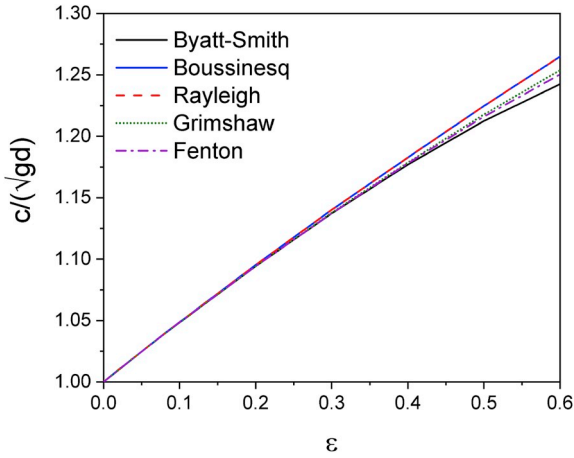


Fig. 4. Theoretical non-dimensionalized phase speeds for the different solitary wave solutions.

#### 4. Description of experiments

The experimental program was carried out at the Hydraulics Laboratory in the Civil Engineering Department of Indian Institute of Technology Bombay. The wave flume measures 50 m in length, 1 m in width and depth, and waves are generated by an electrical motor driven piston-type wavemaker manufactured by HR Wallingford Ltd. The wavemaker piston has a total stroke length of 800 mm. In the middle of the wave flume, a glass wall section of 5 m length offering visual access to the flume from the sides is typically used for visual measurements of wave-structure interaction studies that are carried out. Fig. 5 shows the wave generation system utilized in our study.

Four resistance-type wave gauges, having an operational wave height working range of 600 mm, manufactured by HR Wallingford, measure surface elevation with a spatial resolution of 0.1 mm and sampling rate of 80 Hz. The wave probes were calibrated and the calibration constants were found to repeat with a standard deviation of less than 1%.

As discussed in section 1, when generating solitary waves the origin of the trajectory is shifted to the point  $(-S/2, -\tau/2)$  in the  $x$ - $t$  plane which is behind the midstroke position of the wavemaker piston. Therefore, at the beginning of the solitary wave generation process, the wavemaker must be moved backwards into position—here done by applying a linear motion to the wave paddle over a ramp period of 60 s. The long ramp up period was used to minimize the disturbance of the water surface. In the wave flume, once the ramp up is complete, the piston is held at the beginning position of the solitary wave trajectory for



Fig. 5. Wave generation system at IIT Bombay.

a further 30 s so that the disturbances caused by the ramp dies down. Then the wavemaker piston is allowed to execute the solitary wave trajectory. At the end of the trajectory, the wavemaker piston is held for a further 30 s. Before the next run, the wavemaker piston is brought back to its initial mid-stroke position. To minimize the effects of any unintended disturbances, piston retraction is done linearly in a ramp down duration of 240 s. This ramp profile is illustrated in Fig. 6.

By setting a target amplitude ( $A_{exact}$ ), solitary waves are generated, and the experimental data collected are the measurements of the free surface profiles,  $\eta_{exp}$ , using wave gauges positioned along the wave tank. Solitary waves were generated in a water depth of  $d = 0.3$  m for  $\epsilon$  of 0.1, 0.3 and 0.6. The  $\epsilon$  values are chosen because they represent weak, moderate and high nonlinearity. Water surface displacements during the experiments are measured at fixed locations by wave probes located along the centerline of the wave tank at  $x_1 = 10d$  m,  $x_2 = 30d$  m,  $x_3 = 50d$  m, and  $x_4 = 80d$  m away from the wavemaker. Each experimental run was repeated up to 3 times and a high degree of repeatability was observed—wave elevations measured were repeated to within 0.5% in all cases.

#### 5. Description of the SPH model

The SPH method used here is the same as that discussed in (Valizadeh and Rudman, 2017), which in turn is based on (Monaghan, 1994) and (Monaghan, 2005). It assumes the fluid to be weakly compressible and thus the dynamic pressure  $p$  is related to the density  $\rho$  by an equation of state given by:

$$p = \frac{\rho_0 c_s^2}{\gamma} \left( \left( \frac{\rho}{\rho_0} \right)^\gamma - 1 \right) \quad (22)$$

where  $\rho_0$  is the reference density of the fluid,  $c_s$  is the speed of sound, the value which is chosen to be 10 times greater than the expected maximum flow velocity, and the  $\gamma$  value used here is 7. This ensures that the density fluctuations are small (see (Monaghan, 1994)). In the following discussion, subscripts  $a$  and  $b$  are used for identifying the fluid and boundary particles respectively and  $j$  is used when a summation is over both fluid and boundary particles. The neighborhood of particle  $a$  is defined through non-zero values of the SPH kernel  $W$  and its gradient (taken with respect to the coordinates of particle  $a$ ). The smoothing kernel  $W_{aj} = W(|r_{aj}|, h)$  is a function of the distance between a particle and its neighbor ( $|r_{aj}|$ ) and a smoothing length  $h$  that defines the compact support of each particle. In this paper, we use the fourth-order Wendland kernel described in (Wendland, 1995) with radius  $2h$ . A uniform mean initial particle spacing  $\lambda$ , is used with  $h_j = 1.5\lambda$ . The SPH form of the continuity equation used here is:

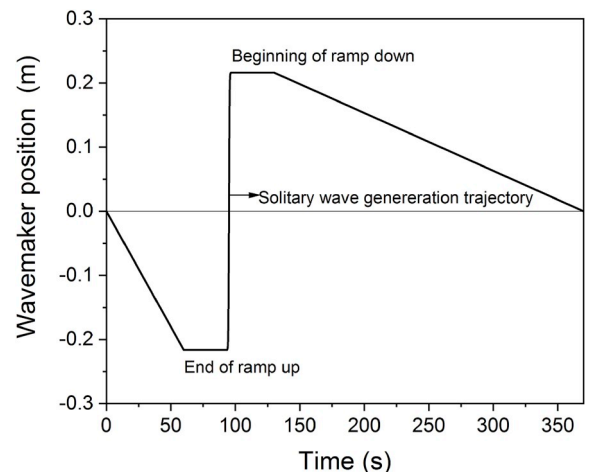


Fig. 6. Typical piston trajectory for solitary wave generation in the laboratory.

$$\frac{d\rho_a}{dt} = \rho_a \sum_j \frac{m_j}{\rho_j} (\mathbf{v}_a - \mathbf{v}_j) \cdot \nabla_a W_{aj} + \zeta \sum_j \frac{m_j}{\rho_j} \frac{\mathbf{r}_{ja}}{|\mathbf{r}_{ja}|^2} \cdot \nabla_a W_{aj} \quad (23)$$

where  $m_a$ ,  $\mathbf{r}_a$ ,  $\mathbf{v}_a$ ,  $\rho_a$ , and  $p_a$  are the mass, position, velocity, density and pressure of particle  $a$  and the summation extends over all particles in its local neighborhood. While the first term on the right-hand side of Eq. (23) is the standard divergence term, the second is a density diffusion term discussed in (Antuono et al., 2012) that removes noise in the density, and hence pressure, fields that is common in weakly compressible SPH formulations. In this term,  $\zeta = 0.2c_s h$  and  $\psi_{ja}$  is:

$$\psi_{ja} = \left\{ (\rho_j - \rho_a) - \frac{1}{2} C_1 \left( \langle \nabla \rho \rangle_j^L + \langle \nabla \rho \rangle_a^L \right) \cdot \mathbf{r}_{ja} \right\}, \quad (24)$$

In Eq. (24),  $C_1$  is a constant that is set to either 1 or 0 and  $\langle \nabla \rho \rangle_j^L$  indicates the renormalised density gradient proposed by Randles and Libersky (1996).

The SPH form of the momentum equation is:

$$\frac{d\mathbf{v}_a}{dt} = - \sum_j m_j \left( \frac{p_a}{\rho_a^2} + \frac{p_j}{\rho_j^2} + \Pi_{aj} \right) \nabla_a W_{aj} + \mathbf{g} \quad (25)$$

In Eq. (25), the summation is over all the particles in the kernel support of particle  $a$  and  $\mathbf{g}$  is the gravitational acceleration. The viscous term is written above as  $\Pi_{aj}$  which is given by

$$\Pi_{aj} = -\alpha \frac{\bar{c}}{\bar{\rho}_{aj}} \frac{\mathbf{v}_{aj} \cdot \mathbf{r}_{aj}}{|\mathbf{r}_{aj}|}, \quad (26)$$

where,  $\alpha$  is a constant,  $\mathbf{v}_{aj} = \mathbf{v}_a - \mathbf{v}_j$ ,  $\mathbf{r}_{aj} = \mathbf{r}_a - \mathbf{r}_j$ ,  $\bar{\rho}_{aj} = (\rho_a + \rho_j)/2$  denotes the average density, and  $\bar{c} = (c_a + c_j)/2$  is the average speed of sound for particles  $a$  and  $j$ . The constant  $\alpha$  can be written in terms of the kinematic viscosity where Kajtar and Monaghan (2010) found for the fourth order Wendland kernel:

$$\nu = \frac{1}{8} \alpha h \bar{c}. \quad (27)$$

This choice of viscous term is justified in the analysis of (Colagrossi et al., 2011).

The fluid particle position is determined by integrating

$$\frac{d\mathbf{r}_a}{dt} = \mathbf{v}_a \quad (28)$$

using the Verlet symplectic method (see (Monaghan, 2005) for a description of this scheme).

Walls have been modelled using 3 layers of fixed fluid particles. To accurately approximate the pressure gradient in the fluid phase near the boundary, the pressure and velocity of boundary particles must be interpolated from the surrounding fluid particles via Eq. (29) and Eq. (30), respectively.

$$p_b = \frac{\sum_a p_a W_{ba}}{\sum_a W_{ba}}, \quad (29)$$

$$\mathbf{v}_w = 2\mathbf{v}_b - \frac{\sum_a \mathbf{v}_a W_{ba}}{\sum_a W_{ba}}, \quad (30)$$

In these equations,  $\mathbf{v}_b$  is the prescribed wall velocity (which is here always set to zero). The density of the wall particle is then obtained from  $p_j$  by inverting the equation of state (Eq. (22)). This density, pressure and velocity are used in the interpolations when calculating the momentum equation. At the free surface, no special pressure boundary conditions are required because the pressure follows directly from the density which is determined from Eq. (23).

In the SPH method, the particle volume is a function of the particle mass and density. The particle masses are fixed at the initial time and then taken as constant during the system evolution. Thus the global mass

is conserved exactly. However, the density of the particle does change according to Eq. (23), and therefore the total volume might not be conserved. From our SPH simulations, it is seen that only very small oscillations in volume are present and that the volume is conserved to within 0.025%. Further details on the WCSPH model used in this study can be found in (Valizadeh and Rudman, 2017).

In order to demonstrate the applicability of the WCSPH model for long term simulation of surface waves, we have studied the evolution of an inviscid standing wave in a rectangular tank and recorded the water surface elevation at its centre. This benchmark test has been used in the past (see Antuono et al., 2011, 2015; Farhadi et al., 2016; Suzuki et al., 2007) to validate free surface numerical methods. In the following discussion  $L_s$  indicates the wavelength of the standing wave and  $k_s$  the corresponding wave number (i.e.  $k_s = 2\pi/L_s$ );  $A_s$  and  $d_s$  represent the amplitude of the standing wave and the equilibrium water depth respectively;  $\varepsilon_s$  denotes the ratio  $2A_s/d_s$  and  $\omega_s$  is the angular frequency which is determined from the dispersion relation for gravity waves:  $\omega_s^2 = gk_s \tanh(k_s d_s)$ . For small-amplitude inviscid waves, the following analytical solution is given by potential theory:

$$\varphi(x, y, t) = -\varepsilon_s \frac{A_s g}{2\omega_s} \frac{\cosh[k_s(y + d_s)]}{\cosh(k_s d_s)} \cos(k_s x) \cos(\omega_s t) \quad (31)$$

The initial configuration of the benchmark test is shown in Fig. 7. Here, at time  $t = 0$ s the free surface is horizontal. The time derivative of the velocity potential ( $\nabla \varphi$ ) has been set to zero in the whole domain and is used to initialize the numerical simulation. Under these conditions, the pressure field is purely hydrostatic. Snapshots of the pressure field during the evolution of a standing wave predicted by the WCSPH model is given in Fig. 8.

The standing wave elevation at the centre of the wave tank for a duration of 10 wave periods has been plotted in the top panel of Fig. 9. It can be clearly seen from this figure that the damping of the wave elevation caused by the diffusive term in the continuity equation is quite small. We have also compared our numerically estimated standing wave elevations with the second-order analytical solution for standing wave elevations described in (Khanna, 1978). A good agreement between the two was recorded. This is shown in the bottom panel of Fig. 9.

To determine the optimum number of particles required to model the fluid, the dissipation ( $A_{est}$ ), normalized by  $A_{exact}$  at various nondimensional distances along the flume is plotted in Fig. 10 for different resolutions. In this figure,  $n_y$  refers to the number of particles used to model the water depth in the wave tank. From Fig. 10 it is observed that the amplitude of the wave declines linearly with  $x$ . At  $x = 80d$ , the wave

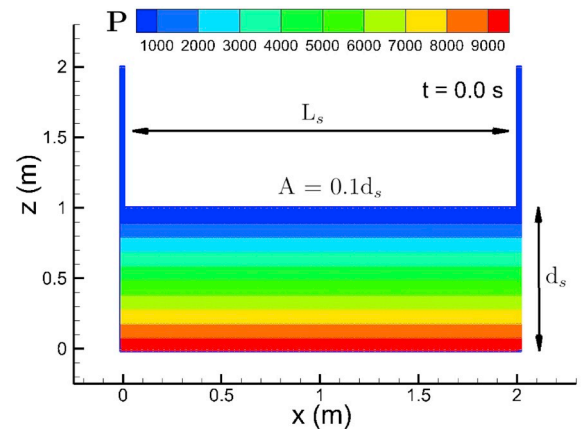
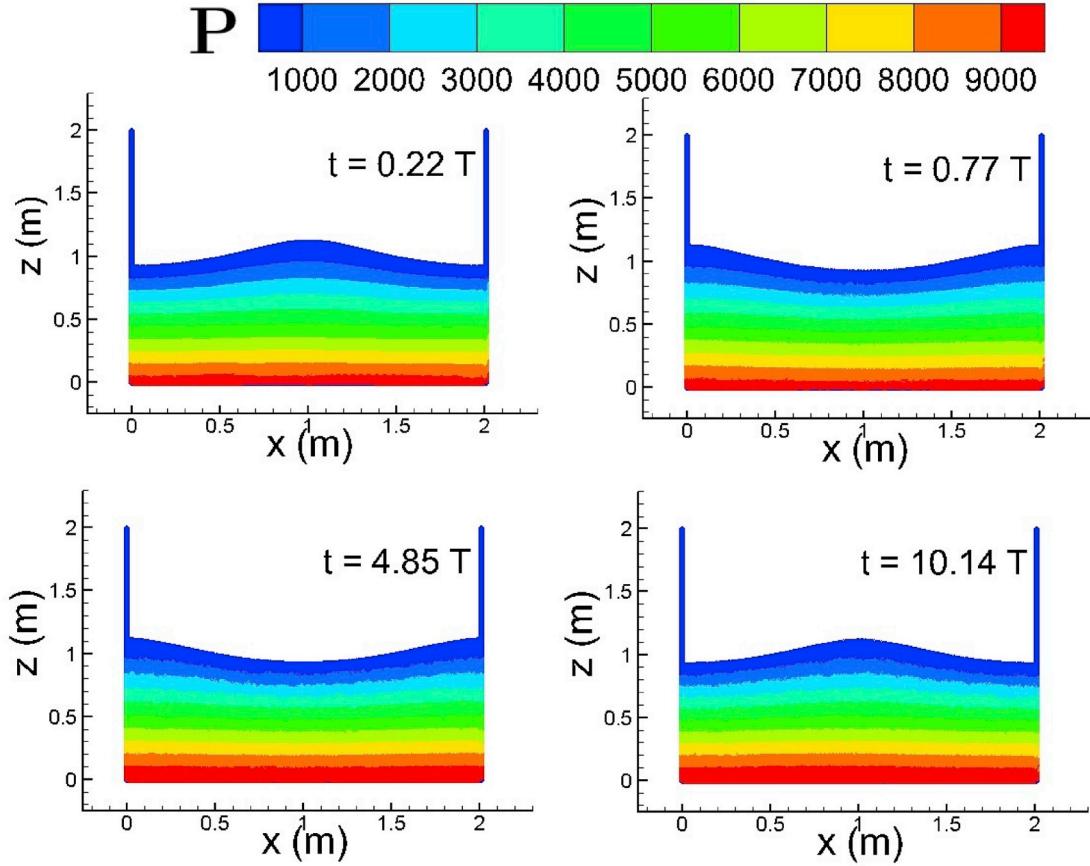


Fig. 7. Initial conditions for the standing wave benchmark test with  $L_s = 2m$  and  $d_s = 1m$ . At  $t = 0$ s, the free surface is flat and the pressure field is hydrostatic. The color bar is of pressure ( $P$ ) in Pa. (For interpretation of the references to color in this figure legend, the reader is referred to the Web version of this article.)



**Fig. 8.** Snapshots of the evolution of a standing wave predicted by the WCSPH model. The SPH particles have been colored using pressure. Here,  $T$  is the standing wave period and the color bar is of pressure ( $P$ ) in Pa. (For interpretation of the references to color in this figure legend, the reader is referred to the Web version of this article.)

amplitude is 26.7%, 25%, 9.7%, 7.1%, 7% and 3.5% smaller than  $A_{exact}$  for  $ny = 25, 32, 50, 64, 75$  and  $100$  respectively. Based on this— $ny \geq 64$  gives acceptable, although non-zero, values of wave dissipation—in this study we have used 64 particles in the vertical direction to model the water depth.

In the numerical simulations, the tank length is  $100d$  in the streamwise direction and  $2d$  in the vertical direction. We have used a total of  $\approx 430,000$  particles in the simulation. The fluid has a density of  $1000 \text{ kg/m}^3$ . Measurements of the water surface elevations are estimated numerically at locations that correspond to the experimental wave gauges.

Snapshots of the pressure (refer panels a, d, g and j of Fig. 11) and velocity fields during the propagation of a solitary wave as predicted by the WCSPH model is given in Fig. 11. Here, we have used the Boussinesq solution along with the GM of wave generation to demonstrate the flow field contours at various locations for a solitary wave of  $\epsilon = 0.3$ . These simulation results also highlight the symmetrical behavior of the vertical component of velocity under the solitary wave (see panels c, f, i and l of Fig. 11).

## 6. Results and discussion

In this section, the characteristics of the four solitary wave solutions generated using the two generation methods are presented. Experimental and numerical results are discussed based on the degree of nonlinearity—low, intermediate, and high—associated with the solitary wave and the comparisons are based on the following parameters: free surface profiles and wave celerity. When examining the free surface profiles, in addition to predicting the target wave amplitude, the

stability of the main pulse and the magnitude of the trailing waves have also been considered. The stability of a solitary wave has been evaluated by studying the changes occurring in the wave profile during propagation between  $x = 10d$  and  $x = 80d$ . The performance of the GM and the MMTM has been compared by recording the wave profiles at  $x = 80d$  away from the wavemaker.

### 6.1. Damping and stability of the main pulse

Our experimental and simulation results show that the wave amplitude declines along the length of the wave tank. This loss of wave amplitude has been recorded in (Goring, 1979), (Katell and Eric, 2002). A major reason for this in the experiments is frictional damping occurring at the bottom and side walls of the wave flume and in numerical simulations it is also due to numerical damping. The frictional damping in experiments has been investigated extensively in the past by Keulegan in (Keulegan, 1948) and Naheer in (Naheer, 1978). According to the theoretical derivation in (Keulegan, 1948), the amplitude attenuation of solitary waves due to boundary layer effect may be calculated from:

$$\left(\frac{A}{d}\right)^{-\frac{1}{4}} = \left(\frac{A_i}{d}\right)^{-\frac{1}{4}} + \frac{1}{12} \left(1 + \frac{2d}{B}\right) \sqrt{\frac{\nu}{g^{\frac{1}{2}} d^{\frac{3}{2}}}} \frac{x}{d} \quad (32)$$

where,  $A_i$  is the initial wave height,  $\nu$  is the kinematic viscosity of the fluid and  $x$  is the distance traveled by the solitary wave in a wave tank of width  $B$ . In this study, Eq. (32) has been used to examine the damping of the various solitary wave profiles.

At low  $\epsilon$  values it was observed that there is hardly any discernible difference between the two generation methodologies (less than 1% in all cases) in both experiments and simulations (refer Fig. 12). In both

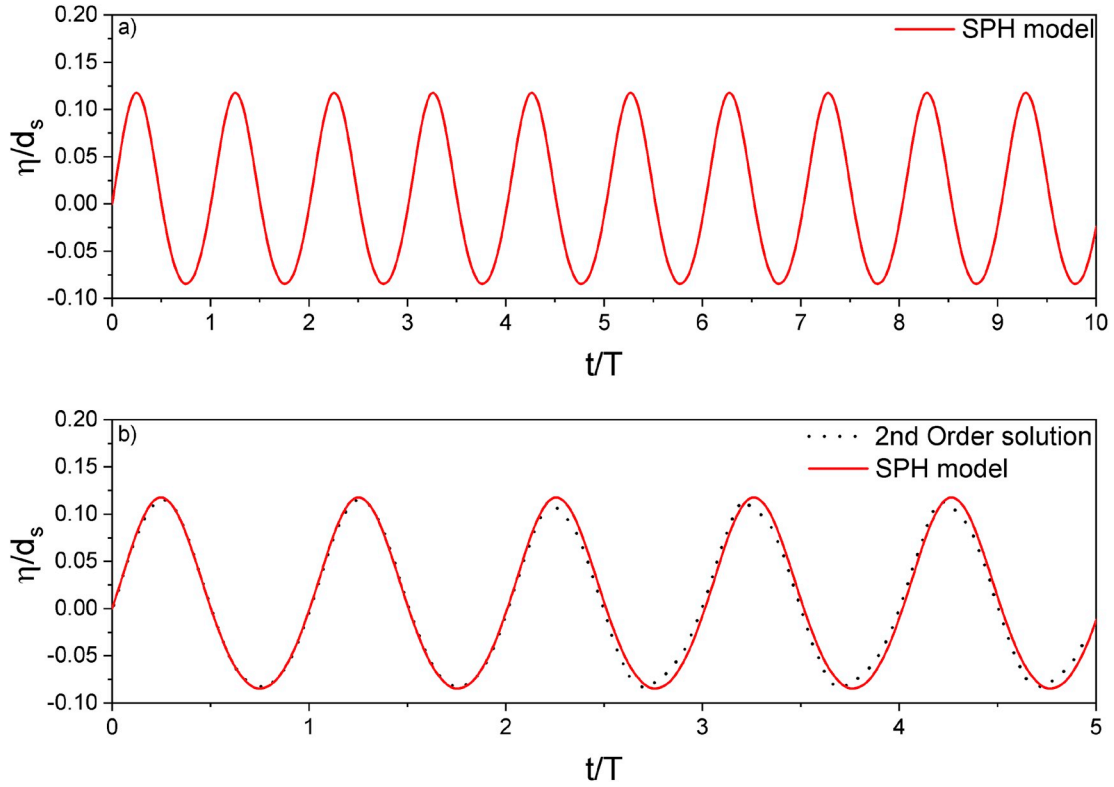


**Fig. 9.** Wave elevation at the tank centre during the evolution of a standing wave.  $\eta$  is the instantaneous wave elevation and  $T$  is the standing wave period. These results indicate that WSPH model is capable of reproducing the exact form of a simple standing wave in long term simulations.

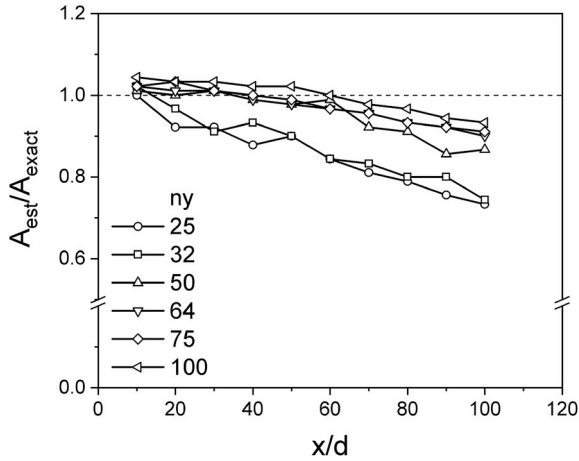


**Fig. 10.** Solitary wave amplitudes estimated at different horizontal positions from the wavemaker: comparison of different resolutions. As can be seen,  $ny \geq 64$  gives acceptable values of wave dissipation.

experiments and simulations, the Rayleigh solution is better at predicting the target amplitude than the other solutions for  $\varepsilon = 0.1$ . The Rayleigh solution gives a damping (over  $\Delta x = 80d$ ) of 21.3% in the experiments and 5% in SPH simulations, whereas the Keulegan formula given in Eq. (32) gives an estimation of 4%. It was observed that the wave amplitude estimated from simulations is closer to the target than that measured from experiments. This is shown in Fig. 13. In this figure, the horizontal dotted line represents the target relative wave height ratio. Since qualitatively there is no discernible difference between the GM and the MMTM at this nonlinearity, we have used the GM in Fig. 13 to highlight our results.

For intermediate  $\varepsilon$  values, the MMTM gave a better description of the

target wave amplitude than the GM in the experiments (5% difference for Rayleigh solution and 6.5% for Boussinesq, Grimshaw and Fenton solutions). Among the four solutions tested, the Rayleigh solution gives the best performance with the measured amplitude being only 9.33% lower than the target amplitude. In our SPH simulations also the Rayleigh solution gave better predictions of the target wave amplitude than the other solutions (only 4% lower), but, for this case alone, the GM was superior to the MMTM (by 13%). From Keulegan's formula, the amplitude decrease over  $\Delta x = 80d$  would be 5.3%. Fig. 14 shows the measured Rayleigh profiles when the generated wave reaches the wave probes located  $80d$  away from the wavemaker in both experiments and SPH simulations. In this figure, the horizontal dotted line represents the target relative wave height ratio, the curve in black represents the GM of wave generation and the curve in red refers to the MMTM of wave generation.

For steep solitary waves ( $\varepsilon = 0.6$ ) in the experiments, our results indicate that there is no significant difference between GM and MMTM (less than 1% in all cases). All four solutions significantly under-predict the target wave amplitude, with the Rayleigh solution being the best (29.27% lower than the target). Interestingly, there is a significant difference between the GM and the MMTM in our SPH results. While the MMTM gives better results than the GM for the Boussinesq, Grimshaw and Fenton solutions (4%, 5% and 5.27% respectively), the reverse is true for the Rayleigh solution (40.9% difference). All solutions demonstrate significant discrepancies in predicting the target amplitude and the best results are obtained from the Rayleigh solution using GM (15.3% more than target), whereas the estimation from Keulegan's formula is 6.3%. In order to confirm our SPH results for the Rayleigh solution using GM, we have carried out simulations at a different water depth ( $d = 0.2$  m). It is seen that at both water depths, for  $\varepsilon = 0.6$ , wave profiles estimated from the SPH simulations at  $80d$  are consistent with this over-prediction as highlighted in Fig. 15.

From both experiments and simulations, it was determined that the Rayleigh solution gave the best description of the target wave amplitude



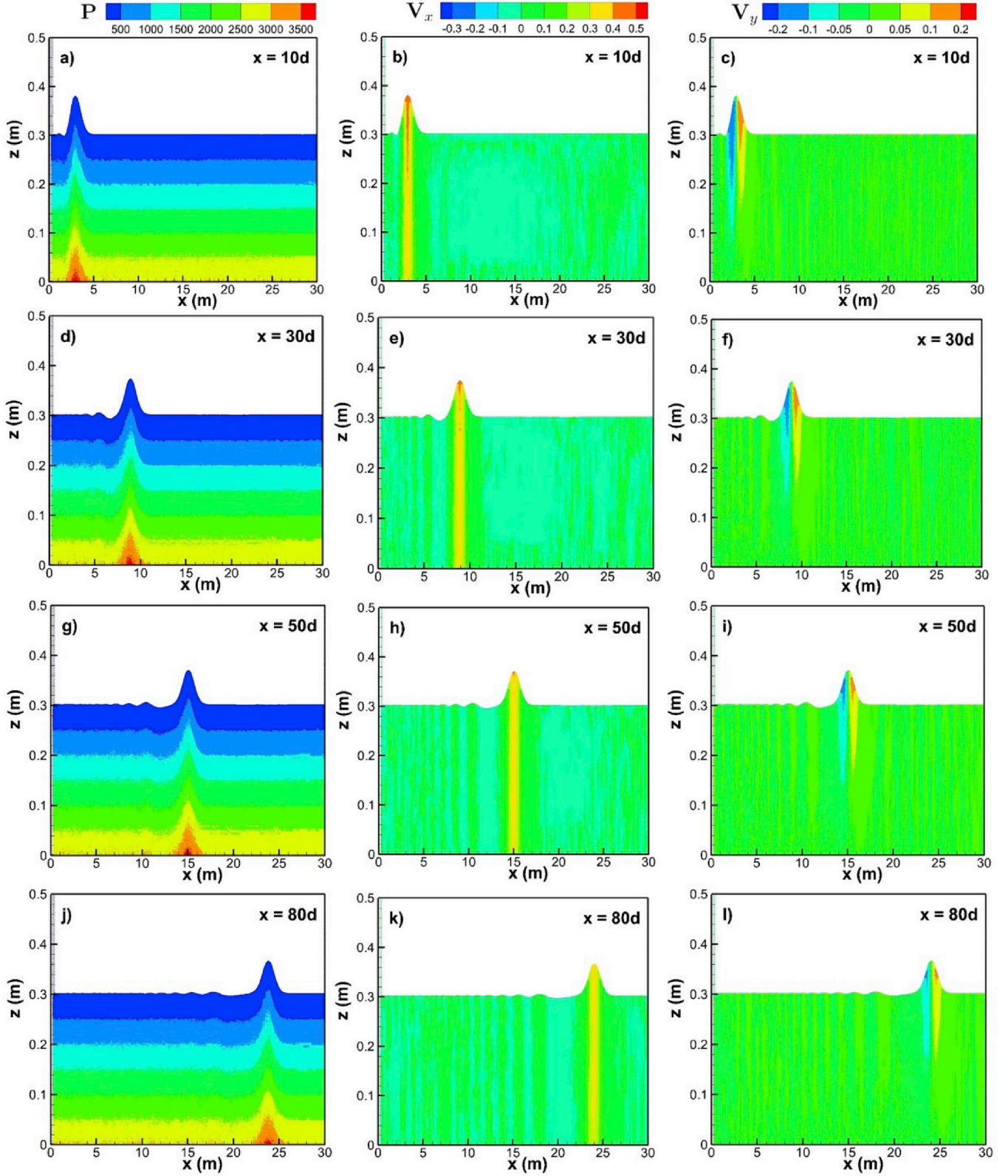
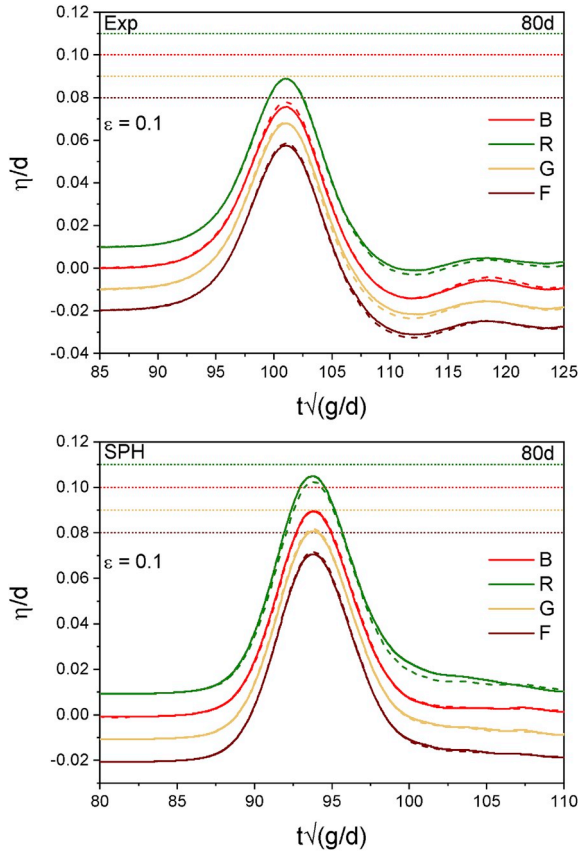


Fig. 11. Snapshots of the evolution of a solitary wave as predicted by the WCSPH model.

always. With increasing  $\epsilon$ , the measured amplitude damping values are higher than those predicted by Keulegan's formula. This observation is consistent with the experimental results in (Liu et al., 2006). It was also noticed that the wave amplitudes estimated from the SPH simulations are much better than those measured from experiments in predicting the

target amplitudes. This is because, in the experiments, there is some water leakage through the small gaps between the wavemaker and the walls of the wave flume. The uncertainties in wave generation due to water leakage around the wavemaker has been reported in the past by Grilli in (Grilli et al., 2004), Wu in (Wu et al., 2016) and Francis in



**Fig. 12.** Wave profiles for  $\varepsilon = 0.1$  at  $80d$ : A comparison between GM (solid line) and MMTM (dashed line) results for all solutions in experiments (top) and simulations (bottom). The colored dotted line is the target wave amplitude corresponding to each solution. There is no noticeable difference between GM and MMTM generated wave profiles in both experiments and simulations.

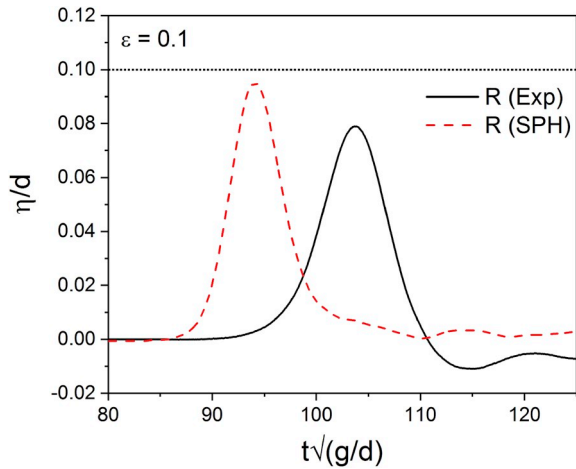


**Fig. 13.** Rayleigh wave profiles for  $\varepsilon = 0.1$  at  $80d$ : A comparison between experiment and SPH simulation results —The simulation results clearly give a better prediction of the target amplitude.

(Francis et al., 2019). To confirm the effect of water leakage past a wavemaker, SPH simulations with a gap between the wave paddle and the bottom wall of the flume were run. These results are shown in Fig. 16. Our simulation results indicate that a gap which is just 0.5% the width of the wave tank causes almost a 14% reduction in the generated wave amplitude. According to (Grilli et al., 2004), when generating higher amplitude waves, the water exerts more pressure on the

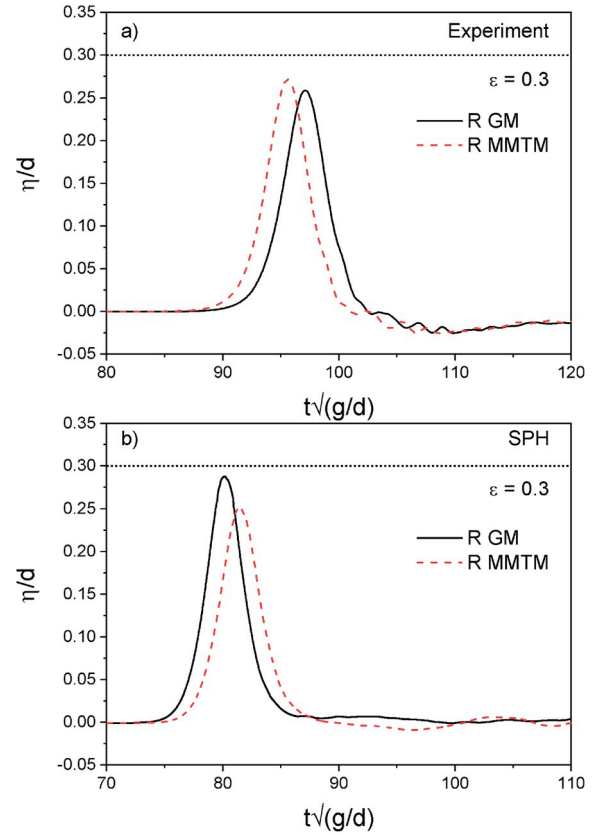


**Fig. 14.** Rayleigh wave profiles for  $\varepsilon = 0.3$  at  $80d$ : A comparison between GM and MMTM for (a) experiments and (b) SPH simulations —While the MMTM outperformed the GM in predicting the target amplitude in the experiments, the reverse is true in our SPH simulations.

wavemaker, which leads to greater leakage past the wavemaker. Therefore, as was observed in our experiments, when generating steeper waves, large volumes of water flows behind the wavemaker and the discrepancy between the target amplitude and the measured wave amplitude becomes more pronounced. Our experimental results indicate that the MMTM outperforms the GM at predicting the target amplitudes, while the reverse is true in the SPH simulations. It is conjectured that this discrepancy is also related to the water leakage occurring past the wavemaker in the experiments and which does not occur in SPH. In the MMTM, as per theory, during the generation of the leading half of the solitary wave profile, the velocity of the wavemaker is lower than the GM (refer Fig. 1). Thus, the volume of water that seeps behind the wavemaker is less in MMTM, which leads to a better description of the target wave amplitude by MMTM in the experiments.

In both experiments and simulations, for all cases studied, it was observed that the solitary wave amplitude recorded at  $10d$  away from the wavemaker, differs from the target amplitude prescribed to the wavemaker to generate it. This indicates that irrespective of the solitary wave solution and the generation methodology used, a wave of an incorrect amplitude is initially generated with an amplitude that is different from the desired amplitude. Therefore the amplitude damping results recorded  $80d$  away from the wavemaker should be adjusted to account for this error in initial conditions. Therefore, the stability of the solitary wave pulse over  $x = 10d$  and  $x = 80d$  has been evaluated by setting the wave amplitude estimated at  $x = 10d$  as  $A_{exact}$ .

To evaluate stability, we have calculated a relative error percentage ( $A_R$ ), defined as:  $\frac{A_x - A_{exact}}{A_{exact}} * 100$ , where  $A_x$  is the measured amplitude of the wave at a particular location,  $x$ . In Fig. 17 we plot the loss of amplitude between  $x = 10d$  and  $x = 80d$  in both experiments and simulations for  $\varepsilon = 0.3$ . In this figure, the solid lines correspond to the GM of wave

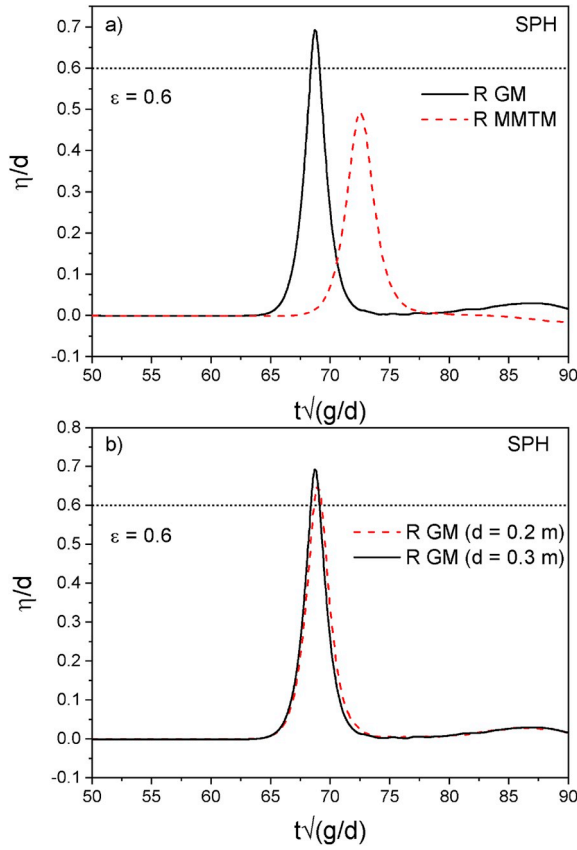


**Fig. 15.** SPH wave profiles for  $\varepsilon = 0.6$  at  $80d$  for the Rayleigh solution. (a) A comparison between GM and MMTM shows the former over-predicting the target amplitude. (b) This over-prediction of the target amplitude when using the GM is also recorded at a different water depth.

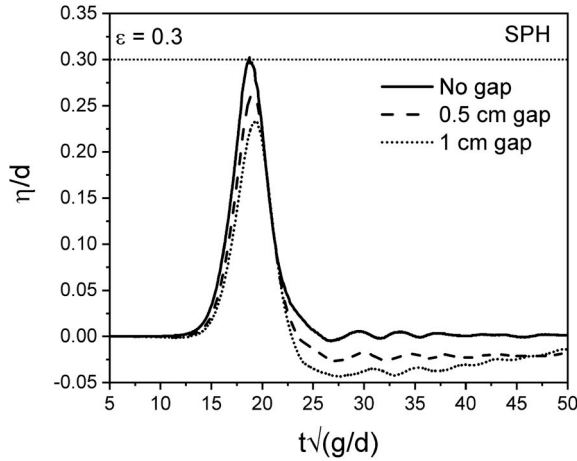


**Fig. 16.** SPH wave profiles with water leakage past the wavemaker: A comparison between numerically estimated wave profiles with different gap width introduced between the wave paddle and the bottom wall of the wave tank. Discrepancy between the target amplitude and the generated wave amplitude is obvious for even a gap width of 0.5 cm.

generation, the dashed lines correspond to the MMTM of wave generation and the dotted line is a reference line indicating perfect stability of the leading pulse.

The experimental results indicate that the Rayleigh solution results in wave pulses whose amplitude decreases the least. From the SPH results it can be seen that the Rayleigh solution results in solitary wave

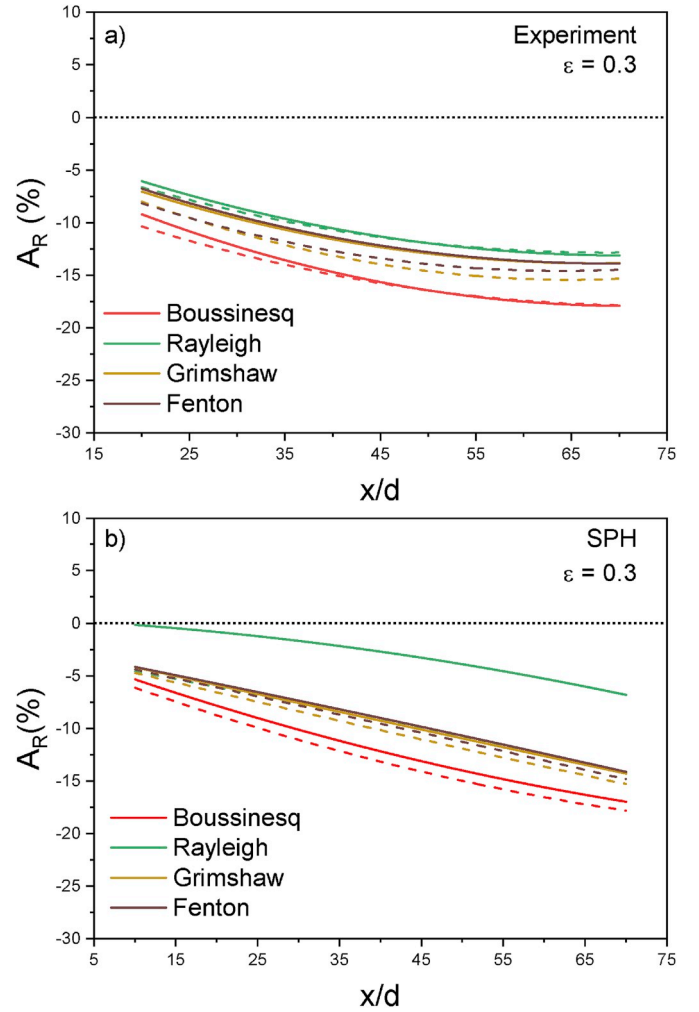


**Fig. 17.** (a) Experimental and (b) numerical loss of amplitude of the main solitary wave pulse over  $x \in [10d, 80d]$

profiles whose amplitude decreases less over  $\Delta x = 70d$  than in the case of those by other solutions, with the GM outperforming the MMTM. Additionally, it is noticed that the Boussinesq solution results in severely damped main pulses during propagation in both experiments and simulations.

Our results for the stability of solitary waves measured between  $x = 10d$  and  $x = 80d$  for  $\varepsilon = 0.1$  and  $\varepsilon = 0.6$  are qualitatively similar to our results at intermediate nonlinearity and are not shown. Thus, from the results, it may be concluded that the stability of the solitary wave depends on which solitary wave solution is being applied and also on the method of solitary wave generation used.

## 6.2. Trailing waves and profile shape

In all experimentally and numerically generated solitary waves, small undulating trailing waves are also produced, indicating that the generated wave is an inexact solitary wave. The magnitude of these perturbations is an indicator of the error in the resulting soliton. In Table 1 we present the amplitude ( $a'$ ) of the undulating trailing wave—either peak or trough—closest to the main pulse of the solitary wave from both experiments and simulations recorded at  $x = 80d$  away from the wavemaker.

For all  $\varepsilon$  values studied, in both experiments and simulations, the Rayleigh solution gives the smallest trailing waves at  $x = 80d$ , with the GM outperforming the MMTM.

The deviations of the generated wave profiles from the theoretical



**Table 1**

Relative amplitude of the trailing waves.

Nonlinearity	Case	$a'/A_{exp}$ (Experiment)	$a'/A_{est}$ (SPH simulations)
$\varepsilon = 0.1$	B GM	0.1872	0.0334
	B MMTM	0.1786	0.0371
	R GM	0.1093	0.0310
	R MMTM	0.1644	0.0324
	G GM	0.1482	0.0331
	G MMTM	0.1714	0.0327
	F GM	0.1422	0.0331
	F MMTM	0.1595	0.0291
$\varepsilon = 0.3$	B GM	0.1553	0.0628
	B MMTM	0.1479	0.0693
	R GM	0.0863	0.0243
	R MMTM	0.0943	0.0359
	G GM	0.1127	0.0349
	G MMTM	0.1155	0.0464
	F GM	0.1154	0.0319
	F MMTM	0.1091	0.0421
$\varepsilon = 0.6$	B GM	0.0961	0.0937
	B MMTM	0.0996	0.0918
	R GM	0.0419	0.0033
	R MMTM	0.0428	0.0115
	G GM	0.0915	0.0731
	G MMTM	0.0981	0.0805
	F GM	0.0914	0.0626
	F MMTM	0.0925	0.0717

bell-shape of solitary waves is another indicator of the accuracy and purity of the generated soliton. Therefore, in order to compare the shape of the generated wave profiles with the theory, surface elevations have been estimated at  $x = 10d$  and  $x = 80d$ . The results of these comparisons are presented in Fig. 19. It is to be noted that we have used only our SPH simulation results in making these comparisons. This is so that the water leakage in our wave generation experiments, as referred to in the earlier section, do not affect the conclusions derived from this study.

Our SPH simulation results indicate that the shape of the wave profiles for all cases are qualitatively similar except for when the Rayleigh solution is used along with GM of wave generation. This is highlighted for  $\varepsilon = 0.3$  in Fig. 18. Hence, in Fig. 19, we have used the Rayleigh solution generated using MMTM to represent the profile shapes for the rest of the cases. Analytical wave profiles at  $x = 10d$  have been plotted based on the amplitude estimated at  $x = 10d$  of Rayleigh solution generated by GM. Similar analytical plots are also made at  $x = 80d$ . It is to be noted here that we have constructed our analytical wave profiles at each location based on the GM Rayleigh amplitudes in order

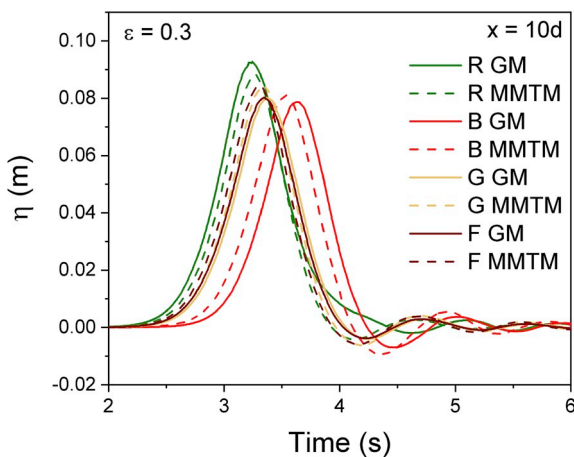


**Fig. 18.** SPH wave profiles for  $x = 10d$ . A comparison between GM and MMTM profiles for all solutions. Wave profile shapes—especially the trailing part—appear similar except for when the Rayleigh solution is used along with GM.

to highlight better the deviations from the theoretical bell-shape. Consistent deviations from theory are observed.

For low  $\varepsilon$  values it is seen that the numerically estimated profiles are in consistent agreement with only negligible difference between the Rayleigh solution generated using GM and the other solutions. At  $x = 10d$ , the generated wave profile shape closely matches the theoretical profile with only minor differences occurring at the front and rear of the leading pulse. After covering a distance of  $\Delta x = 70d$ , a small extended shelf region forms behind the numerically estimated soliton (refer Fig. 19). In addition, the frontal part of the estimated wave profile at this location differs significantly from theory.

For intermediate  $\varepsilon$  values, the numerical profiles in all cases differ from the theoretical profiles noticeably at both the front and rear of the wave at both  $x = 10d$  and  $x = 80d$ . For the Rayleigh solution generated using GM, a prominent shelf region forms behind the main pulse of the soliton, which disappears by the time the wave reaches  $x = 80d$ . In all the other cases, immediately after generation, the main peak of the solitary wave is followed by a depression below the still water level, which separates from the main wave pulse before it reaches  $x = 80d$ .

In the case of higher amplitude solitary waves, the characteristics of the wave profile shapes estimated are noticeably different to those estimated for  $\varepsilon = 0.1$ . While in the former all the profiles have a sharp crest with steep side slopes and a broad base, the latter is associated with a rounded crest and a more gentle side slope. The mass of the trailing shelf that forms behind the solitary wave pulse in the case of the Rayleigh solution generated through GM is more, and it is similar to the  $\varepsilon = 0.3$  case, where it vanishes by the time the wave reaches  $x = 80d$ . In the remaining cases, the depression below the still water level recorded at  $x = 10d$  is mild and is completely absent at  $x = 80d$ .

In our SPH simulations it was observed that as the wave propagates, the trailing waves separate from the main peak of the soliton indicating that the celerity of the trailing wave is smaller than that of the generated solitary wave. This separation process happens over shorter distances when steeper waves are generated—for higher amplitude waves the celerities of the generated peaks are larger—and maybe considered as a progression towards an exact solitary wave. As can be seen in Fig. 19, the numerical profile shapes deviate from the theoretical shapes and the extent of the deviation depends on the degree of nonlinearity. All the solitary wave solutions assume that during propagation, energy is conserved by the soliton. However, in our SPH model, it loses energy due to dissipation which manifests as a change in the shape of the wave profile.

### 6.3. Wave celerity

The wave celerity associated with a solitary wave solution is used to determine the depth-averaged horizontal water particle velocity which is then matched to the velocity of the wavemaker in GM and also during the generation of the trailing half of the soliton in MMTM. Therefore, in order to generate an exact solitary wave, an accurate choice of the wave celerity parameter is required. A perfect solitary wave would have a celerity which is identical to the theoretical celerity of the exact solution given by Byatt-Smith in (Byatt-Smith, 1970).

Experimental and numerical celerities have been calculated by dividing the distance between the wave probes placed at  $x = 10d$  and  $x = 80d$  with the time taken by the wave to travel this distance. In Table 2, we have compared the deviations ( $\delta$ ), of the experimental and numerical wave celerities from the estimate given by Byatt-Smith.

In both experiments and numerical simulations, the celerities of the generated Rayleigh-type waves are closer to the celerity estimates of the exact solitary wave as compared to the celerities of the waves generated by the application of the other solutions. Moreover, when applying the Rayleigh solution, on average, a better agreement with the Byatt-Smith estimates is obtained in the experiments when using the MMTM, whereas in our SPH simulations it is upon using the GM. Consequently, the wave profiles in the experiments are more accurate when the former



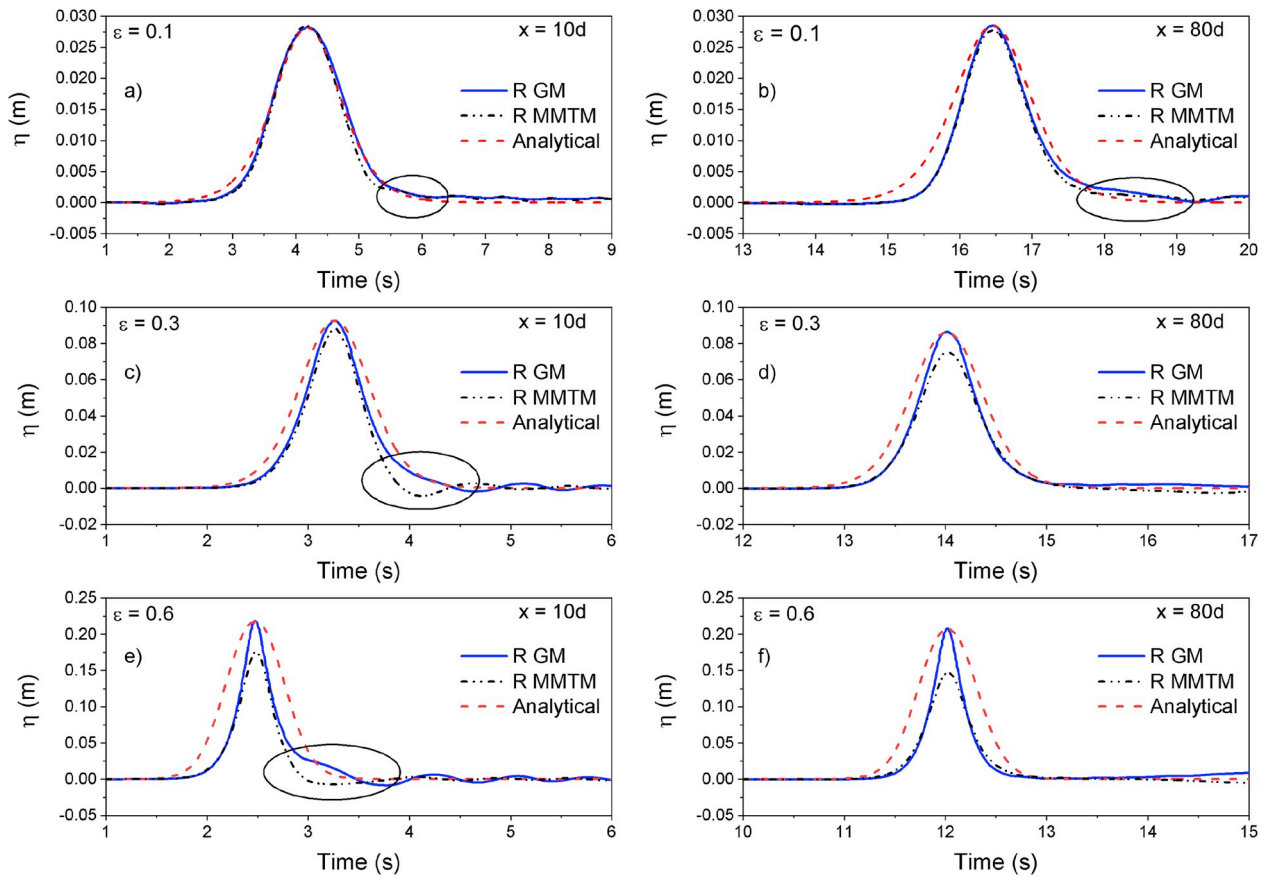


**Fig. 19.** SPH wave profiles for  $x = 10d$  (left) and  $80d$  (right). A comparison between GM, MMTM and analytic profiles for the Rayleigh solution —The GM method clearly provides better amplitude fidelity. Trailing waves that are obvious at  $x = 10d$  have mostly separated from main peak by  $80d$ , although discrepancies are clearly seen, especially for low  $\epsilon$ .

**Table 2**  
Deviations in celerity from Byatt-Smith estimate.

Nonlinearity	Case	$\delta$ % (Experiment)	$\delta$ % (SPH simulations)
$\epsilon = 0.1$	B GM	2.58	-0.9
	B MMTM	2.53	-0.33
	R GM	2.48	-0.04
	R MMTM	2.33	-0.14
	G GM	3.19	-0.52
	G MMTM	2.5	-0.14
	F GM	3.09	-0.4
	F MMTM	2.33	-0.14
	F GM	2.33	-0.14
$\epsilon = 0.3$	B GM	1.59	-2.83
	B MMTM	1.65	-2.39
	R GM	1.39	0.15
	R MMTM	1.3	-1.24
	G GM	1.38	-2.30
	G MMTM	1.65	-1.95
	F GM	1.65	-2.12
	F MMTM	1.65	-1.86
	F GM	1.65	-1.86
$\epsilon = 0.6$	B GM	-3.66	-5.91
	B MMTM	-3.42	-5.43
	R GM	-1.2	2.34
	R MMTM	-1.2	-1.97
	G GM	-3.25	-5.59
	G MMTM	-3.01	-4.78
	F GM	-3.17	-5.35
	F MMTM	-3.17	-4.46
	F MMTM	-3.17	-4.46

is used while the numerically estimated wave profiles are better when the latter is applied.

## 7. Conclusions

The aim of this study was to determine the solitary wave solution and the generation methodology that gives the most stable and pure solitary waves in large-scale experiments and numerical SPH simulations using a piston-type wavemaker. In this paper, we have tested the solitary wave solutions of Boussinesq (B), Rayleigh (R), Grimshaw (G) and Fenton (F) using Goring's method (GM) and also the method of Malek-Mohammadi and Testik (MMTM) for  $\epsilon$  values ranging from 0.1 to 0.6 with  $d = 0.3$  m. Each solitary wave profile generated was analyzed based on the amplitude of the main pulse, stability, amplitude of the trailing waves and the celerity. Comparisons were also made between the experimental observations and the SPH simulation results. It was noticed that none of these solitary wave generation procedures resulted in an exact solitary wave. Nonetheless, the following conclusions can be drawn from the range of  $\epsilon$  studied:

1. The pureness of the generated solitary wave depends heavily on which solitary wave solution is being used, and, in both our experiments and numerical simulations, for all  $\epsilon$  values, the Rayleigh-type solitary wave gave the best performance amongst the various solutions considered.
2. GM for solitary wave generation used along with the Rayleigh solution gives the best performance in numerical models. The waves generated in this case display the least damping, are more stable and are associated with the smallest trailing waves. It was determined that when using the GM and the Rayleigh solution, celerity values of

the resulting profiles come closest to the estimate of an exact solitary wave given by Byatt-Smith in (Byatt-Smith, 1970).

3. In the experiments also the Rayleigh-type solitary wave gave better predictions of the characteristics of the target solitary wave. However, here it was the MMTM which yielded more accurate solitary wave profiles when compared to the GM.

Our results indicate that the generation methodology that resulted in the most fidelity in experiments cannot always be carried across to our numerical SPH model. It is conjectured that this discrepancy is due to water leakage around the wave paddle in the physical wave flume.

Hence, based on our results we would recommend the application of the Rayleigh-type solitary wave in both experiments and numerical simulations. With respect to the wave generation methodology to be used, we suggest the GM in numerical models and also in physical wave tanks where the water leakage and the effect of surface contaminants is non-existent. But, for physical wave flumes similar to ours, we would prescribe the MMTM for solitary wave generation.

These recommendations, based on the different solitary wave parameters studied, are expected to be useful in various experimental and numerical studies involving solitary waves, for eg: in the study of solitary wave reflection and the interaction of solitary waves with structures. As we have focused on solitary wave profiles at distances of 80 water depths away from the wavemaker, the results from our study are expected to benefit studies involving solitary waves in long laboratory setups.

#### CReditor author statement

**Vivek Francis (VF):** Conceptualization, Methodology, Software, Investigation, Formal analysis, Validation, Visualization, Writing – Original draft preparation. **Balaji Ramakrishnan (BR):** Methodology, Supervision, Funding acquisition, Writing – Review & Editing. **Murray Rudman (MR):** Methodology, Supervision, Funding acquisition, Writing – Review & Editing. **Alireza Valizadeh (AV):** Methodology, Software.

#### Declaration of competing interest

The authors declare that they have no known competing financial interests or personal relationships that could have appeared to influence the work reported in this paper.

#### Acknowledgements

This research was funded by the Australia-India Strategic Research Fund through grant AISRF06240.

#### Appendix A. Supplementary data

Supplementary data to this article can be found online at <https://doi.org/10.1016/j.coastaleng.2020.103633>.

#### References

- Altomare, C., González-Cao, J., Dominguez, J.M., Crespo, A.J.C., Gómez-Gesteira, M., Lomonaco, P., 2017. Generation of trains of tsunami-like solitary waves in DualSPHysics model. In: Proceedings of the 12th International SPHERIC Workshop, Ourense, 13–15 June 2017. Universidade de Vigo, Spain, no. June, pp. 83–89.
- Antuono, M., Colagrossi, A., Marrone, S., Lugni, C., 2011. Propagation of gravity waves through an sph scheme with numerical diffusive terms. *Comput. Phys. Commun.* 182 (4), 866–877.
- Antuono, M., Colagrossi, A., Marrone, S., 2012. Numerical diffusive terms in weakly-compressible SPH schemes. *Comput. Phys. Commun.* 183 (12), 2570–2580.
- Antuono, M., Marrone, S., Colagrossi, A., Bouscasse, B., 2015. Energy balance in the  $\delta$ -sph scheme. *Comput. Methods Appl. Mech. Eng.* 289, 209–226.
- Boussinesq, J., 1871. “Théorie de l’intumescence liquide appelée onde solitaire ou de translation se propageant dans un canal rectangulaire. *CR Acad. Sci. Paris* 72, 755–759.
- Byatt-Smith, J., 1970. An exact integral equation for steady surface waves. *Proceedings of the Royal Society of London. A. Mathematical and Physical Sciences* 315 (1522), 405–418.
- Byatt-Smith, J.G.B., Longuet-Higgins, M.S., 1976. On the speed and profile of steep solitary waves. *Proc. R. Soc. Lond.* 350 (1661), 175–189.
- Clamond, D., Germain, J., 1999. Interaction between a Stokes wave packet and a solitary wave. *Eur. J. Mech. B Fluid* 18 (1), 67–91.
- Colagrossi, A., Antuono, M., Souto-Iglesias, A., Le Touze, D., 2011. Theoretical analysis and numerical verification of the consistency of viscous smoothed-particle-hydrodynamics formulations in simulating free-surface flows. *Phys. Rev.* 84.
- Daily, J.W., Stephan, S.C., 1952. The solitary wave. *Coastal Engineering Proceedings* 13–50.
- Farhadi, A., Ershadi, H., Emdad, H., Goshtasbi Rad, E., 2016. Comparative study on the accuracy of solitary wave generations in an ISPH-based numerical wave flume. *Appl. Ocean Res.* 54, 115–136.
- Fenton, J., 1972. A ninth-order solution for the solitary wave. *J. Fluid Mech.* 53, 257–271.
- Francis, V., Ramakrishnan, B., Rudman, M., 2019. Solitary wave interaction with vertical porous barriers. In: 38th International Conference on Ocean, Offshore and Arctic Engineering OMAE. ASME.
- Gedik, N., Irtem, E., Kabadasi, S., 2005. Laboratory investigation on tsunami run-up. *Ocean. Eng.* 32 (5–6), 513–528.
- Goring, D.G., 1979. *Tsunamis: The Propagation of Long Waves onto a Shelf*. PhD Thesis. California Institute of Technology.
- Goseberg, N., Wurpts, A., Schlurmann, T., 2013. Laboratory-scale generation of tsunami and long waves. *Coast Eng.* 79, 57–74.
- Grilli, S., Gilbert, R., Lubin, P., Vincent, S., Astruc, D., Legendre, D., Duval, M., Kimmoun, O., Branger, H., Devrard, D., et al., 2004. Numerical modeling and experiments for solitary wave shoaling and breaking over a sloping beach. In: 14th International Offshore and Polar Engineering Conference IGARSS, vol. 3. ISOPE.
- Grimshaw, R., 1971. The solitary wave in water of variable depth. Part 2. *J. Fluid Mech.* 46 (3), 611–622.
- Hsiao, S.C., Lin, T.C., 2010. Tsunami-like solitary waves impinging and overtopping an impermeable seawall: experiment and RANS modeling. *Coast Eng.* 57 (1), 1–18.
- Kajtar, J.B., Monaghan, J.J., Sept, 2010. On the dynamics of swimming linked bodies. *Eur. J. Mech. B Fluid* 29, 377–386.
- Katell, G., Eric, B., 2002. Accuracy of solitary wave generation by a piston wave maker. *J. Hydraul. Res.* 40 (3), 321–331.
- Keulegan, G.H., 1948. Gradual damping of solitary waves. *Nat. Bur. Sci. J. Res* 40, 487–498. June.
- Khanna, S.B., 1978. Standing waves of finite amplitude on surface of ideal liquid of finite depth. *Fluid Dyn.* 13 (2), 187–191.
- Liang, D., Gotoh, H., Khayyer, A., Chen, J.M., 2013. Boussinesq modelling of solitary wave and N-wave runup on coast. *Appl. Ocean Res.* 42, 144–154.
- Liu, P.-F., Simarro, G., Vandever, J., Orfila, A., 2006. Experimental and numerical investigation of viscous effects on solitary wave propagation in a wave tank. *Coast Eng.* 53 (2–3), 181–190.
- Malek-Mohammadi, S., Testik, F., 2010. New methodology for laboratory generation of solitary waves. *J. Waterw. Port, Coast. Ocean Eng.* 136, 286–294. October.
- Monaghan, J.J., 1994. Simulating free surface flows with SPH. *J. Comput. Phys.* 110, 399–406.
- Monaghan, J.J., 2005. Smoothed particle hydrodynamics. *Rep. Prog. Phys.* 68 (8), 1703.
- Naheer, E., 1978. The damping of solitary waves. *J. Hydraul. Res.* 16 (3), 235–249.
- Randles, P.W., Libersky, L.D., 1996. Smoothed particle hydrodynamics: some recent improvements and applications. *Comput. Methods Appl. Mech. Eng.* 139, 375–408.
- Rayleigh, L., 1876. On waves. *Phila. Mag.* 1, 257–259.
- Suzuki, Y., Koshizuka, S., Oka, Y., 2007. Hamiltonian moving-particle semi-implicit (hmps) method for incompressible fluid flows. *Comput. Methods Appl. Mech. Eng.* 196 (29–30), 2876–2894.
- Svendsen, I.A., 1974. Cnoidal Waves over a Gently Sloping Bottom. Institute of Hydrodynamics and Hydraulic Engineering.
- Synolakis, C.E., 1987. The runup of solitary waves. *J. Fluid Mech.* 185, 523–545.
- Temperville, A., 1985. Contribution à la théorie des ondes de gravité en eau peu profonde.
- Teng, M.H., 1997. Solitary wave solution to boussinesq equations. *J. Waterw. Port, Coast. Ocean Eng.* 123 (3), 138–141.
- Valizadeh, A., Rudman, M., 2017. A numerical approach for simulating flow through thin porous media. *Eur. J. Mech. B Fluid* 65, 31–44.
- Wendland, H., 1995. Piecewise polynomial, positive definite and compactly supported radial functions of minimal degree. *Adv. Comput. Math.* 4 (1), 389–396.
- Wu, N.J., Tsay, T.K., Chen, Y.Y., 2014. Generation of stable solitary waves by a piston-type wave maker. *Wave Motion* 51 (2), 240–255.
- Wu, N.J., Hsiao, S.C., Chen, H.H., Yang, R.Y., 2016. The study on solitary waves generated by a piston-type wave maker. *Ocean. Eng.* 117, 114–129.
- Yeh, H., Liu, P., Briggs, M., Synolakis, C., 1994. Propagation and amplification of tsunamis at coastal boundaries. *Nature* 372 (6504), 353.